Space–Time Spectral Analysis of the Southern Hemisphere Daily 500-hPa Geopotential Height

CHENG SUN

State Key Laboratory of Numerical Modeling for Atmospheric Sciences and Geophysical Fluid Dynamics (LASG), Institute of Atmospheric Physics, Chinese Academy of Sciences, and Graduate University of Chinese Academy of Sciences, Beijing, China

JIANPING LI

State Key Laboratory of Numerical Modeling for Atmospheric Sciences and Geophysical Fluid Dynamics (LASG), Institute of Atmospheric Physics, Chinese Academy of Sciences, Beijing, China

(Manuscript received 18 January 2012, in final form 6 June 2012)

ABSTRACT

In this paper the authors use the NCEP–Department of Energy (DOE) Reanalysis 2 (NCEP2) data from 1979 to 2004 to expand the daily 500-hPa geopotential height in the Southern Hemisphere (SH, 90°–20°S) into a double Fourier series, and analyze the temporal frequency characteristics of the expansion coefficients over various spatial scales. For the daily series over the whole year, the coefficient series of the extratropical-mean height is characterized by a significant low-frequency (10–30 day) variation. For zonal waves with $(k, l) = (1–5, 1)$, where k and l are the zonal and meridional wavenumbers, respectively, the low-frequency variability is most pronounced for zonal wavenumbers 3 and 4; while the short wave with zonal wavenumber 5 has significant high-frequency (4–8 day) variability. For meridional waves with $(k, l) = (0, 2–6)$, the meridional dipole ($l = 2$) makes a major contribution to the low-frequency variability, consistent with the intraseasonal space–time features of the southern annular mode (SAM). The meridional tripole ($l = 3$) also exhibits low-frequency variability. For two-dimensional waves $(k, l) = (1–5, 2–6)$, the dipole is a preferred meridional structure for intraseasonal modes with large zonal scales, indicating an out-of-phase relationship between low-frequency planetary-scale waves at mid- and high latitudes. The diagnostic results outlined above can be explained, to a certain extent, by the dispersion relation for Rossby waves. Theoretical analysis indicates that zonal wavenumber 3, zonally symmetric flow such as SAM, and planetary-scale waves with meridional dipole structures may be interpreted as low-frequency eigenmodes of the atmosphere.

1. Introduction

Because of its important influence on regional and hemispheric climates (Kidson 1988; Simmonds 2003), many recent studies have examined the variability of atmospheric circulation in the Southern Hemisphere (SH). For example, Gong and Wang (1999) analyzed variations in sea level pressure (SLP) in the SH, and introduced the southern annular mode (SAM), a hemispheric seesaw pattern in the SLP field associated with a north–south redistribution of atmospheric mass between mid- and high latitudes. Thompson and Wallace (2000) conducted a further investigation into the three-dimensional (3D) structure of SAM, reporting nearly zonally symmetric vacillations in the extratropical zonal flow, and an equivalent barotropic structure in the vertical direction. Li and Wang (2003) proposed the concept of the annular belt of actions (ABA) to represent zonally symmetric fluctuations, and established the SAM index (SAMI; Nan and Li 2003; Wu et al. 2009; Feng et al. 2010), which gives an improved description of the zonal symmetry of SAM. However, SAM also has zonally asymmetric components linked to the El Niño–Southern Oscillation

Corresponding author address: Dr. Jianping Li, State Key Laboratory of Numerical Modeling for Atmospheric Sciences and Geophysical Fluid Dynamics (LASG), Institute of Atmospheric Physics, Chinese Academy of Sciences, P.O. Box 9804, Beijing 100029, China.
E-mail: ljp@lasg.iap.ac.cn

DOI: 10.1175/MWR-D-12-00019.1

(ENSO; Fan 2007; Wang et al. 2008; Pezza et al. 2012) and to the asymmetric feedback of synoptic eddies (Codron 2007). This asymmetric component of SAM in the South Pacific also has an impact on rainfall in Australia (Meneghini et al. 2007). SAM shows an approximately 10-day time scale (Gerber et al. 2008; Gong et al. 2010) and is active on a submonthly scale (Li and Li 2009).

Zonal wave 3 (ZW3) is an important mode in geopotential height and wind fields in the SH, and is characterized by zonal asymmetries associated with zonal wavenumber 3. ZW3 is a dominant feature in the extratropics and reaches maximum amplitudes near 50°S (van Loon and Jenne 1972; Raphael 2004). Previous studies have shown that ZW3 plays an important role in blocking (Trenberth and Mo 1985), and makes a strong contribution to monthly and interannual variability in teleconnections (Trenberth 1980). The signal of ZW3 is dominant over submonthly (Mo and Ghil 1987; Hansen and Sutera 1991) and seasonal (Mo and White 1985) time scales. Dell'Aquila et al. (2007) associated ZW3 with low-frequency (20–40 day) variability using space–time spectral analysis (Hayashi 1979). van Loon and Jenne (1972) noted that the existence of ZW3 is linked to the land–sea distribution in the SH; however, it remains unknown whether ZW3 is an internal mode of the atmosphere, or a mode induced by lower boundary forcing [sea surface temperature (SST), sea ice cover, topography, etc.].

Besides SAM and ZW3, the Pacific–South American (PSA or PSA1) pattern is the dominant teleconnection in the South Pacific linked with ENSO (Mo and Higgins 1998). It resembles its Northern Hemisphere (NH) counterpart, the Pacific–North American (PNA) mode, and behaves like a wave train associated with the anomalous tropical convection during ENSO (Turner 2004). The PSA pattern can be found in the second empirical orthogonal function (EOF) mode of monthly-mean 500-hPa geopotential height anomalies (Schneider et al. 2004). The PSA is pronounced on various time scales ranging from intraseasonal to interannual (Mo and Higgins 1998; Mo and Paegle 2001; Cai and Watterson 2002). While the PSA mode may originate from the tropics, it has also been identified as an internal mode of the atmosphere (Frederiksen and Webster 1988).

The spatial patterns of synoptic atmospheric circulation in the NH are associated mainly with zonal wavenumbers 5–7 (Blackmon et al. 1984; Jin et al. 2006a). The behavior of SH 500-hPa synoptic systems is far less well investigated than those systems in the NH (Keable et al. 2002). Moreover, the above studies show that the spatial scales of circulation patterns are linked to their time scales. Systematic studies are required to investigate the nature of this space–time connection, and to develop a better understanding of circulation variability in the SH.

Space–time spectral analysis is an effective tool with which to investigate the space–time characteristics of atmospheric circulation. In early studies, information was obtained by a one-dimensional (1D) Fourier analysis of the field at a given latitude or of the latitudinally averaged field, followed by computation of the time–power spectrum of each spatial Fourier component (Kao 1968; Hayashi 1979; Dell'Aquila et al. 2007). However, the meridional structure is also important, meaning that a two-dimensional (2D) spatial spectral decomposition should be considered (Blackmon 1976; Jones and Simmonds 1993). Blackmon (1976) used a spherical harmonic expansion to investigate the space–time characteristics of waves in the entire NH. As the spherical harmonic decomposition can only be performed on an entire sphere, he assumed the geopotential height field to be an even function of latitude about the equator and reflected the NH daily geopotential height onto the SH. As a result of this limitation, spherical harmonics are of little use for the decomposition of atmospheric fields over the extratropics. Recently, double Fourier series (DFS) expansion has been used to analyze and solve numerical computation problems on a sphere (Cheong 2000, 2006; Layton and Spotz 2003; Cheong et al. 2004). These studies indicate that spherical harmonics and DFS only differ in their choice of expansion functions in latitude. Spherical harmonics use associated Legendre functions, while DFS use the Fourier series. The Fourier series are much simpler, and may have some advantages in their application to the extratropical region given an appropriate choice of Fourier modes. Although the DFS method is widely used in numerical computations, research into its application in space–time spectral analysis of observation data is limited. Therefore, this study aims to perform a space–time spectral analysis on the geopotential height using the DFS approach.

Few investigations have been performed into the space–time spectral characteristics of daily atmospheric circulation fields over the southern extratropics using a 2D spatial spectral decomposition. What are the space–time characteristics of the SH intraseasonal atmospheric variability in wavenumber–frequency space? Analysis of the space–time spectra of the SH daily atmospheric circulation will give us a more comprehensive understanding of the intraseasonal variability of large-scale circulation patterns in the SH. Furthermore, it is necessary to examine the time-scale dependence of the SH circulation patterns at different spatial scales using daily data for a better understanding of their typical time scales. Thus, new insight will be

gained into the dynamics of the important climate modes identified by the DFS expansion.

The aim of this paper is to analyze the space–time spectral characteristics of the SH (poleward of 20°S) daily atmospheric circulation and their description of large-scale intraseasonal variability. We will also consider the temporal frequency characteristics of 2D planetary waves, which have been previously unreported. For this purpose, we adopt the DFS expansion and standardized power spectrum (Li and Li 2009) that were employed in the companion study that focuses on the NH (Sun and Li 2011). We support previously mentioned studies of the SH teleconnection patterns and their temporal variability. However, in contrast to the previous studies, we also show the following: 1) the extratropical-mean 500-hPa geopotential height exhibits low-frequency variability, 2) there is a constant out-of-phase relationship between low-frequency planetary-scale waves at mid- and high latitudes, and 3) by the use of the dispersion relation for Rossby waves, low-frequency teleconnection patterns (e.g., ZW3 and SAM) can be theoretically interpreted as eigenmodes of the atmosphere.

The remainder of this manuscript is organized as follows. The data and methods are described in section 2, and the results of the spectral analysis are presented in section 3, along with a discussion of the corresponding circulation patterns. In section 4, we interpret the results by applying the dispersion relation, and finally, section 5 presents the conclusions and the outlook for future studies.

2. Data and methodology

a. Data

In this study we used daily-mean 500-hPa geopotential height reanalysis data from the region poleward of 20°S, provided by the National Centers for Environmental Prediction–Department of Energy (NCEP–DOE) Reanalysis 2 (NCEP2; Kanamitsu et al. 2002) for the period from 1 January 1979 to 31 December 2004, and with a spatial resolution of 2.5° × 2.5°. To analyze the variability in geopotential height, we derived daily anomaly data by removing the mean seasonal cycle, which is defined as the annual average and the first four Fourier harmonics of the 20-yr (1980–99) daily climatology. The winter half-year is from May to October, and the summer half-year is from November to April. To use equal area-weighted data in the analyses of geopotential height fields, the gridpoint data were weighted by the square root of the cosine of the geographical latitude before computing the space–time spectra (North et al. 1982).

The daily SAMI used here is defined as the difference in the normalized daily-mean zonal-mean SLP between 40° and 70°S (Nan and Li 2003; Wu et al. 2009; Li and Li 2009; Feng et al. 2010; Blunden et al. 2011), derived from NCEP2 reanalysis data for the period 1979–2004. This SAMI is a modification of the Antarctic Oscillation (AAO) index defined by Gong and Wang (1999), which is the difference in the normalized zonal-mean SLP between 40° and 65°S. The modified SAMI is used because the negative correlation in the zonal-mean SLP anomalies between 40° and 70°S is stronger than that between 40° and 65°S. In addition, the daily AAO index from the Climate Prediction Center (CPC) at NCEP (referred to as SAMI_CPC) is employed to verify the reliability of the results based on the SAMI. The daily SAMI_CPC is constructed by projecting the daily-mean 700-hPa height anomalies onto the leading EOF mode of the monthly-mean 700-hPa height anomalies poleward of 20°S for the SH.

b. Spatial spectral expansion

The daily 500-hPa geopotential height anomaly $Z(\lambda, \phi)$ is considered to be a function of longitude and latitude, where λ is longitude and ϕ is latitude. Following the usual procedure, the function $Z(\lambda, \phi)$ is first expanded by a 1D Fourier series in longitude with truncation K:

$$Z(\lambda, \phi) = \sum_{k=-K}^{K} Z_k(\phi) e^{ik\lambda}, \tag{1}$$

where $Z_k(\phi) = (1/M)\sum_{m=0}^{M-1} Z(\lambda_m, \phi) e^{-ik\lambda_m}$, M is the number of data points along a latitude circle, $\lambda_m = 2\pi m/M$, and k is the zonal wavenumber.

Next we expand $Z_k(\phi)$ in a Fourier series in latitude that accounts for the north–south boundary conditions. The latitude ϕ is defined over (ϕ_0, ϕ_1), and here $\phi_0 = 20°S$ and $\phi_1 = 90°S$. For ease of expansion, $Z_k(\phi)$ is described as $z_k(\Phi)$ by a coordinate transformation, where $z_k(\Phi) = Z_k(\phi)$, Φ is defined over $(0, \pi)$, and $\Phi = [(\phi - \phi_0)/(\phi_1 - \phi_0)]\pi$. Rigid boundary conditions are imposed at both northern and southern boundaries, and $z_k(0) = z_k(\pi) = 0$. Therefore, we expand $z_k(\Phi)$ in a Fourier sine series with truncation L:

$$z_k(\Phi) = \sum_{l=1}^{L} z_{l,k} \sin l\Phi, \tag{2}$$

where $z_{l,k}$ is the Fourier coefficient and is a function of the zonal wavenumber k and the meridional wavenumber l.

Substituting (2) into (1), and using Euler's formula, allows $Z(\lambda, \phi)$ to be represented by a sum of the DFS:

$$\left.\begin{aligned} Z(\lambda,\phi) &= \sum_{k=1}^{K}\sum_{l=1}^{L} C_{k,l}\cos k\lambda \sin l\Phi + \sum_{k=1}^{K}\sum_{l=1}^{L} S_{k,l}\sin k\lambda \sin l\Phi + \sum_{l=1}^{L} R_l \sin l\Phi, \\ \Phi &= \frac{\phi-\phi_0}{\phi_1-\phi_0}\pi, \end{aligned}\right\} \tag{3}$$

where $C_{k,l}$ and $S_{k,l}$ denote the coefficients of zonal cosine and sine waves, respectively, and R_l denotes the coefficient of meridional waves of the zonally symmetric field. In this paper, we adopt $K = 30$ and $L = 25$.

Figure 1a shows the zonal means of the standard deviations of the daily 500-hPa geopotential height, the DFS representation of daily height field and the root-mean-square deviation (RMSD) between the daily observations and the DFS representation. As seen in Fig. 1a, the RMSD values are very small over the extratropical SH, indicating that the daily height fields are well represented by the DFS. The geopotential height fluctuations at the northern boundary appear to be about one order of magnitude smaller than those at midlatitudes, indicating the rigid boundary condition at the northern boundary is reasonable. The area-weighted geopotential height is identically zero at the South Pole, which is consistent with the southern boundary condition of the DFS representation. The annual-mean series of the ratios of the extratropical-mean RMSD to standard deviation (Fig. 1b) shows that the error is always small. Therefore, the representation of daily geopotential height anomaly via DFS is considered to be appropriate.

To focus on the intraseasonal space–time spectral characteristics of the large-scale circulation in the SH, the zonal and meridional wavenumbers are truncated at 5 and 6, respectively. The analysis was conducted under the following conditions: condition 1, $(k, l) = (0, 1)$, the mode for this condition (a spatially homogeneous pattern) represents the extratropical mean of the daily height anomaly; condition 2, $(k, l) = (1–5, 1)$, modes for this condition represent zonal waves; condition 3, $(k, l) = (0, 2–6)$, modes for this condition represent meridional waves of the zonal mean; and condition 4, $(k, l) = (1–5, 2–6)$, modes for this condition represent 2D waves.

c. Standardized power spectrum

Each set of expansion coefficients (C, S, and R), for fixed values of k and l, forms a time series. After obtaining the daily coefficient series, we calculate the standardized power spectrum (Li and Li 2009) to analyze the temporal frequency characteristics at various spatial scales. The procedure for each set of coefficient series is as follows:

1) The series is divided into 26 sections (or years) and a Hamming window is applied to remove the effects of the side lobes that result from the sharp edges of the spectral windows. This gives 26 degrees of freedom for the composite spectrum.
2) The continuous power spectrum S for each section i ($i = 1, \ldots, n$, where n is the total number of years) is then computed. At the same time, the reference red-noise spectrum is determined based on the lag-1 autocorrelation coefficient of the series. The 95% upper confidence limit S_{95} is then estimated from the reference red-noise spectrum based on the χ^2 distribution at the 95% confidence level.
3) The standardized power spectrum in each section is defined as

$$R^* = \frac{S^*}{S_{95}}, \tag{4}$$

where

$$S^* = \begin{cases} S, & S \ge S_{95} \\ 0, & S < S_{95} \end{cases}. \tag{5}$$

Then, the composite standardized power spectrum averaged across all sections can be written as follows:

$$\overline{R^*} = \frac{1}{n}\sum_{i=1}^{n} R_i^*, \tag{6}$$

where $n = 26$. The number of years (or sections) for the corresponding significant periods can be expressed as

$$N = \sum_{i=1}^{n} m_i, \quad m_i = \begin{cases} 1, & S \ge S_{95} \\ 0, & S < S_{95} \end{cases}. \tag{7}$$

Therefore, for a fixed wavenumber (k, l), $\overline{R^*}$ and N are functions of frequency (or period), and can be used to estimate the statistical significance of a certain time period. The $\overline{R^*}$ evaluates the extent to which the signal can be distinguished from red noise, while N measures the frequency of S exceeding S_{95}. Higher values of $\overline{R^*}$ and N indicate that the corresponding period is more

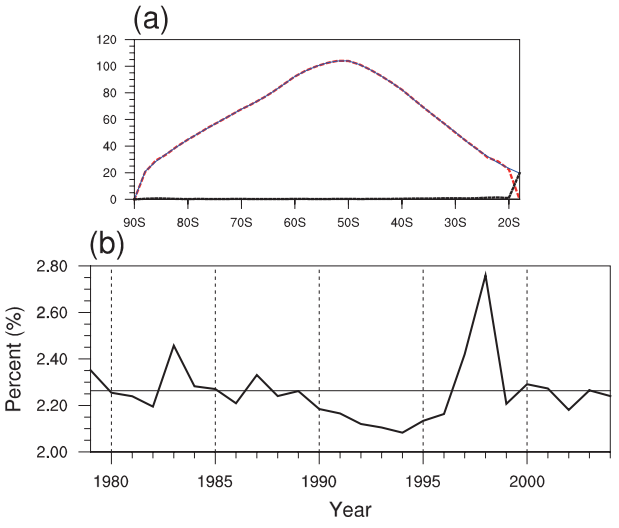

FIG. 1. (a) Zonal means of the standard deviations of daily 500-hPa geopotential height (blue thin line), the DFS representation of daily height field (red dashed line), and the RMSD between the daily observations and the DFS representation (black dashed line) from 1979 to 2004 over the southern extratropics. (b) The annual-mean series of the ratios of the extratropical-mean RMSD to standard deviation of daily 500-hPa geopotential height.

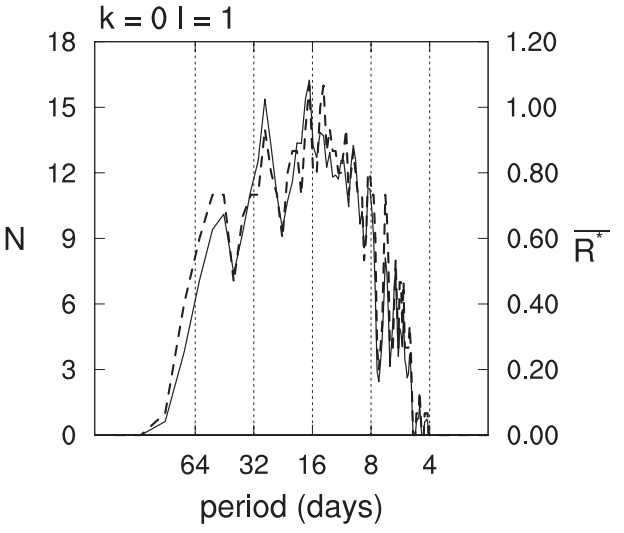

FIG. 2. Composite standardized power spectrum ($\overline{R^*}$, solid line) over the entire year and the number of years (N, dashed line) for significant spectrum periods from 1979 to 2004 at wavenumber $(k, l) = (0, 1)$.

significant. Although these two measures have different physical significances, they both quantify the degree of periodicity in the coefficient series and both provide similar results. Therefore, for simplicity, we only employ N in the comparison of significant periods among different wavenumbers for conditions 2–4. The number of year N for zonal wavenumber k, meridional wavenumber l, and period T is

$$\left.\begin{aligned} N(k, l, T) &= \frac{1}{2}[N(C_{k,l}, T) + N(S_{k,l}, T)], \quad k > 0 \\ N(l, T) &= N(R_l, T), \qquad\qquad\qquad\quad k = 0 \end{aligned}\right\}. \tag{8}$$

If the value of N is near to, or more than, half of the total number of years (here 13), the mode with corresponding spatial wavenumbers is considered to be periodic (or quasi-periodic) in majority of years.

3. Diagnostic analysis

a. Temporal spectral characteristics

Figure 2 shows $\overline{R^*}$ and N for wavenumber $(k, l) = (0, 1)$ (condition 1) over 26 years. Over the time period of 10–30 days, values of $\overline{R^*}$ are high, with most exceeding 0.8, and the maximum value being close to 1.0; values of N are also high, with most being around 12, and the maximum being close to 15. Over this time period, both $\overline{R^*}$ and N show two sharp peaks with periods of 16 and 30 days. These results suggest the daily extratropical-mean geopotential height at 500 hPa displays low-frequency variability with periods of 10–30 days. The results over the 26 winter and summer half-years are similar to those over the 26 full years (not shown), indicating that such low-frequency signals are not seasonally dependent.

Figure 3a shows the spectra of N for wavenumbers $(k, l) = (1–5, 1)$ (condition 2) over 26 years. The various zonal wavenumbers show a range of signals in frequency space. The spectral width of N for $k = 1$ is narrow, and the values of N have two peaks, centered around time periods of around 4 and 10 days, with maximums being close to 10. For $k = 2–4$, the spectral widths of N become much wider, ranging from days to months, and the maximum values occur mainly over periods of around two weeks, with the greatest value exceeding 14. For $k = 5$, the spectral width becomes extremely narrow, and the dominant period is about one week, over which the value of N exceeds 18. It is worth noting that our results shown in Fig. 3a closely resemble the Hayashi spectra for 500-hPa zonal waves obtained by Dell'Aquila et al. (2007, see their Fig. 1a), and moreover, we show the statistically significant periods for different scales of zonal waves.

To characterize the signals in frequency space for different wavenumbers, we integrate N in spectral bands of low (10–30 day) and high (4–8 day) frequencies. Figure 3b shows the series of averaged N with respect to zonal wavenumber k. The value of N averaged in the low-frequency band is most significant for $k = 3$, which is

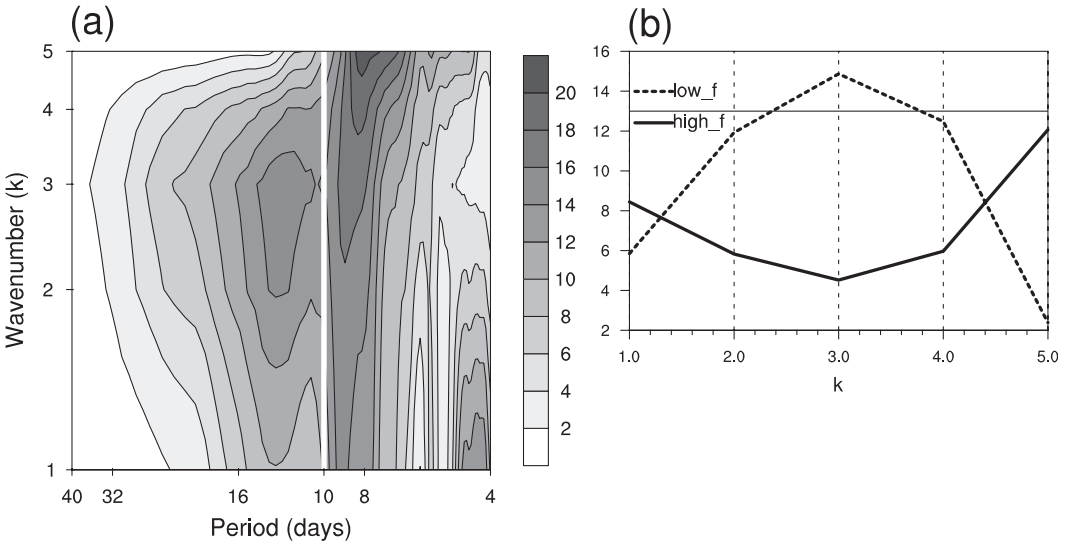

FIG. 3. (a) Spectra of N as a function of period and wavenumber for (k, l) = (1–5, 1) (condition 2). (b) Low-frequency (10–30 day, dashed line) and high-frequency (4–8 day, solid line) band means of N as a function of wavenumber. The horizontal solid line stands for 13 yr.

consistent with the intraseasonal space–time characteristics of ZW3. Therefore, the low-frequency variability of ZW3 (Dell'Aquila et al. 2007) is demonstrated, and this feature is more evident over winter half-years (not shown). Kidson (1999) performed an EOF analysis on the intraseasonal 300-hPa streamfunction in the SH, and found that the two leading EOFs had zonal wavenumber-4 patterns. Figure 3b shows that zonal wavenumber 4 also appears to be low frequency, which is consistent with the findings of Kidson (1999). In addition, besides zonal wavenumbers 3 and 4, zonal wavenumber 2 exhibits mainly low-frequency variability with periods of 10–30 days. We found insignificant differences between low- and high-frequency band-averaged N for $k = 1$, indicating that zonal wavenumber 1 has both low- and high-frequency components. This finding is consistent with the results reported by Randel (1988). The high-frequency variability associated with $k = 5$ suggests that it is a representative spatial scale for synoptic activities.

Figure 4a presents the spectra of N for wavenumbers (k, l) = (0, 2–6) (condition 3) over 26 years. The spectrum signals show large variations associated with different meridional wavenumbers. For $l = 2$–3, the spectral widths of N are relatively wide, ranging from days to months, and maximum values are distributed mainly over the periods of around two weeks, with the greatest value exceeding 16. For $l = 4$–6, the spectral widths of N are narrow, centered around 10 days, and the values are relatively small.

Figure 4b presents the series of band-averaged N with respect to meridional wavenumber l, showing sharp drops in low-frequency band-averaged N among different meridional wavenumbers. For $l = 2$, the low-frequency band-averaged N is the most significant, suggesting low-frequency variability associated with the meridional dipole structure of the zonally symmetric circulation. This finding further demonstrates the intraseasonal variability of SAM (Pohl et al. 2010; Li and Li 2009). Lorenz and Hartmann (2001) reported the second EOF of the zonal-mean zonal wind in the southern extratropics is a meridional tripole, and this EOF mode behaves much like red noise in its power spectrum. Our research shows that the meridional tripole in the zonal-mean geopotential height ($l = 3$) seems to have periods of 10–30 days. The values of band-averaged N for $l = 4$–6 are smaller, suggesting that short meridional waves in the SH do not have preferred periods.

The condition for wavenumbers (k, l) = (1–5, 2–6) (condition 4) is more complicated than conditions 1–3. Figure 5 depicts N for condition 4. Condition 4 can be divided into two groups in terms of the distribution pattern of N, with one group for $k = 1$–3, and the other for $k = 4$–5. For small zonal wavenumbers ($k = 1$–3), the spectral widths of N narrow as meridional wavenumber increases, suggesting that the meridional dipole ($l = 2$) has the broadest range of periods. The relatively large values of N are mainly distributed at periods around, and longer than, 10 days, which we refer to as the low-frequency band, indicating one prominent regime of planetary-scale waves. Over the low-frequency time scales, the value of N decreases as meridional wavenumber increases, implying

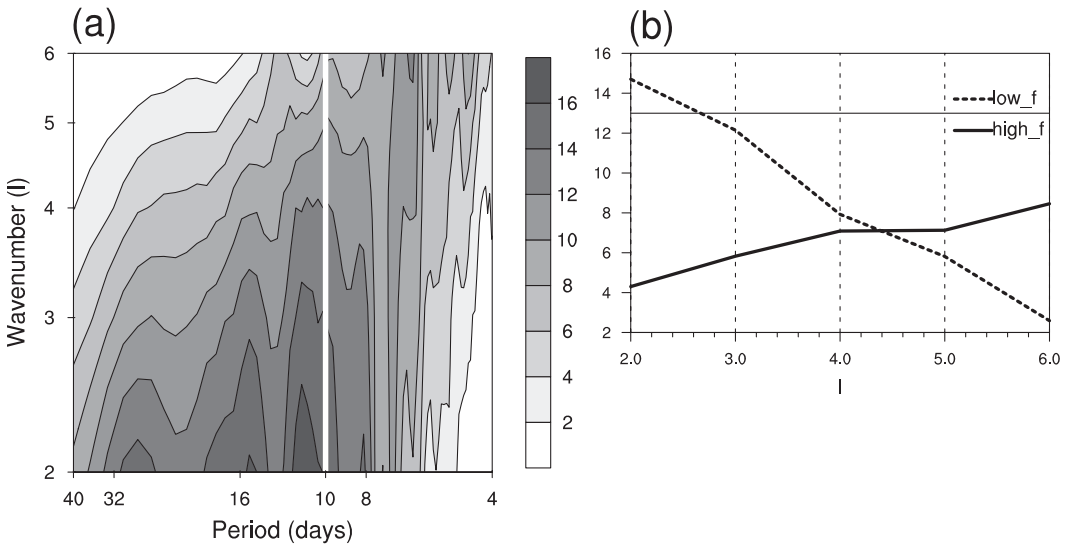

FIG. 4. As in Fig. 3, but for $(k, l) = (0, 2–6)$ (condition 3).

that the meridional structures of low-frequency planetary waves are dominated by south–north dipoles. This result indicates a constant out-of-phase relationship between low-frequency planetary waves (k = 1–3) at mid- and high latitudes, which may be connected with the dipole structure associated with blocking events (Shutts 1983). For small zonal scales (k = 4–5), the values of N are mainly located at time scales shorter than 8 days, which we refer to as the high-frequency band, indicating high-frequency variability associated with these scales of wave.

Figure 6 illustrates the distribution of low-frequency band-averaged N with respect to wavenumbers k and l. It is clear that zonal wavenumber 3 and the meridional dipole are the most important low-frequency patterns in the atmospheric circulation over the southern extratropics, and these features are consistent with the intraseasonal space–time characteristics of ZW3 and SAM. In addition, the meridional tripole, planetary waves with meridional dipole structures and zonal wavenumbers 2 and 4 appear to have mainly low-frequency variability with periods around, and longer than, 10 days.

b. *Space–time analysis of SAM and PSA*

We introduce SAM and PSA to help further explain the results presented in section 3a. The intraseasonal variability of both SAM and PSA is first examined using the daily indices. The PSAI is constructed by projecting the daily-mean 500-hPa height anomalies onto the loading pattern of PSA, which is obtained as the second EOF mode of the monthly-mean 500-hPa geopotential height over the southern extratropics. Figure 7 shows the standardized power spectrum analyses of both SAM and PSA daily indices. Both SAM and PSA exhibit considerable intraseasonal variability with periods of 10–30 days, with the most prominent periodicity having a wavelength of around two weeks. We also performed the standardized power spectrum analysis on the daily SAMI_CPC, and achieved a similar result as that for SAMI (not shown).

The spatial structures of SAM and PSA were further investigated by the use of DFS. The spatial patterns of SAM and PSA were first derived by the regression of daily 500-hPa height anomalies onto the normalized daily SAMI and PSAI, respectively, and then decomposed into the DFS. The leading Fourier modes in the SAM and PSA patterns determined by the DFS expansion are listed in Table 1, together with the associated expansion coefficients. The absolute value of the expansion coefficient measures the contribution from each Fourier mode to the observed pattern. The SAM pattern is dominated by a remarkable zonal symmetry with a meridional dipole structure, while the magnitudes of zonal asymmetries are much smaller, and consist of planetary waves with meridional dipole structures and large-scale zonal waves. The PSA pattern receives major contributions from 2D waves with wavenumbers $(k, l) = (1, 2)$ and $(k, l) = (2, 2)$, and zonal wavenumbers 2 and 3 also contribute to the PSA pattern.

Figure 8 illustrates the spatial patterns of SAM and PSA, and the representations via the Fourier modes listed in Table 1. The representation of the SAM pattern (Fig. 8b) is similar to the observed pattern (Fig. 8a), showing the three weak centers of action located over the South Atlantic, southern Indian, and South Pacific Oceans (Simmonds and King 2004). The Rossby wave train extending from the tropical Pacific to South America associated with PSA (Fig. 8c) is well represented by the combination of

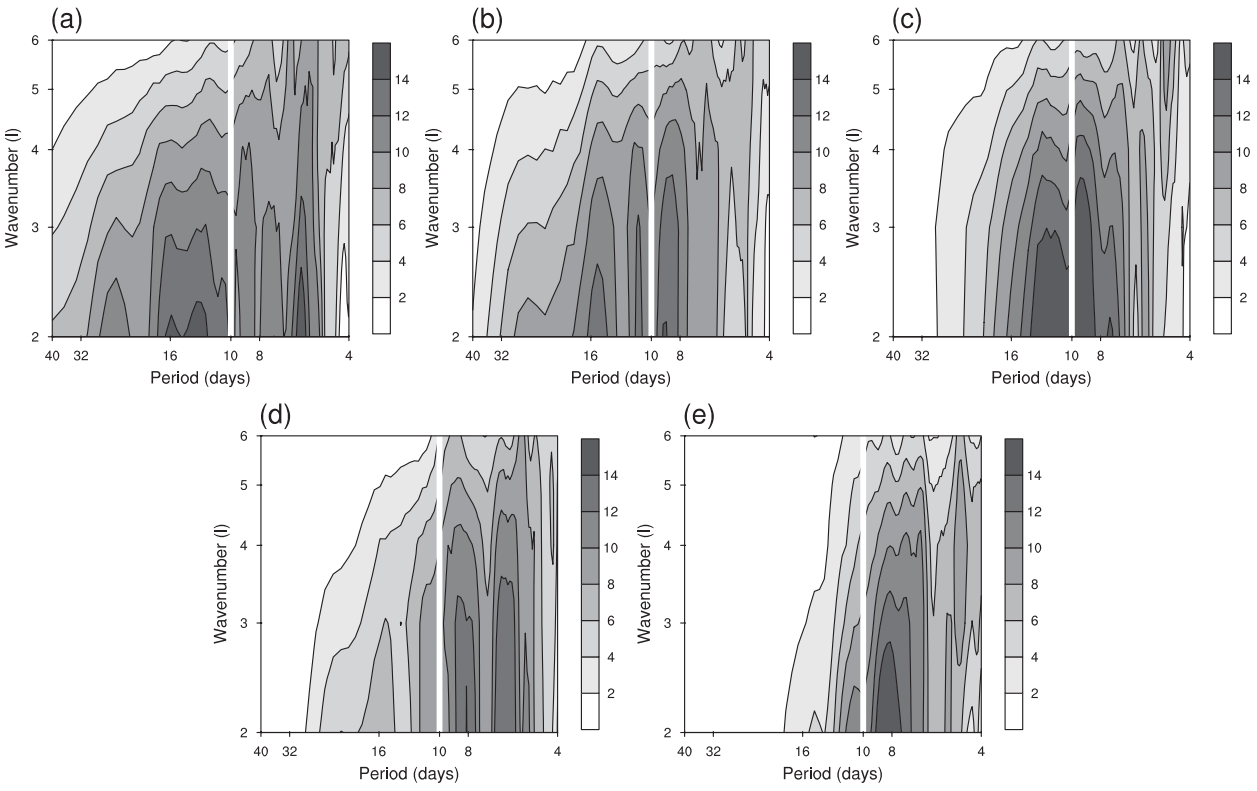

FIG. 5. (a)–(e) As in Fig. 3a, but for $(k, l) = (1, 2–6)$, $(k, l) = (2, 2–6)$, $(k, l) = (3, 2–6)$, $(k, l) = (4, 2–6)$, and $(k, l) = (5, 2–6)$, respectively.

the corresponding Fourier modes (Fig. 8d). The spatial correlation coefficients between represented and observed patterns for both SAM and PSA are around 0.9, implying that the representations via the leading Fourier modes are in strong agreement with the observed patterns. Therefore, the dominant roles of the meridional dipole structure in both SAM and PSA patterns are clearly identified, which indicates that low-frequency modes may favor a dipole structure in the meridional direction. In addition, because of the remarkable intraseasonal variability associated with SAM and PSA, these two modes may contribute to the low-frequency variability of the Fourier modes shown in Table 1, which further supports the results reported in section 3a.

4. Theoretical analysis

The dispersion relation for the perturbation streamfunction of the form $\sin[(\pi l/L_y)y]\exp\{i[(2\pi k/L_x)x - \omega t]\}$ on a Mercator projection of a sphere (Hoskins and Karoly 1981) can be written as

$$\omega = \frac{2\pi k}{L_x}\overline{u}_M - \beta_M \frac{2\pi k}{L_x}\Bigg/\left[\left(\frac{2\pi k}{L_x}\right)^2 + \left(\frac{\pi l}{L_y}\right)^2\right], \quad (9)$$

where ω, $\overline{u}_M$, β_M, R, k, and l denote the angular frequency, background wind speed, meridional gradient of the absolute vorticity in Mercator coordinate, the earth's radius, and zonal and meridional wavenumbers,

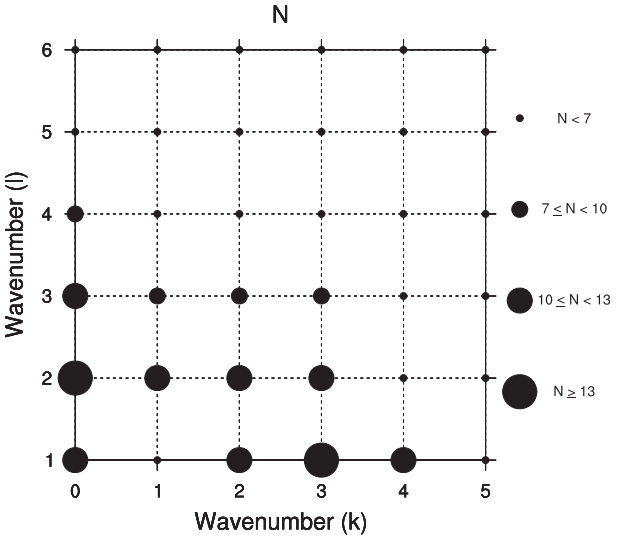

FIG. 6. The distribution of low-frequency band-averaged N with respect to wavenumbers k and l.

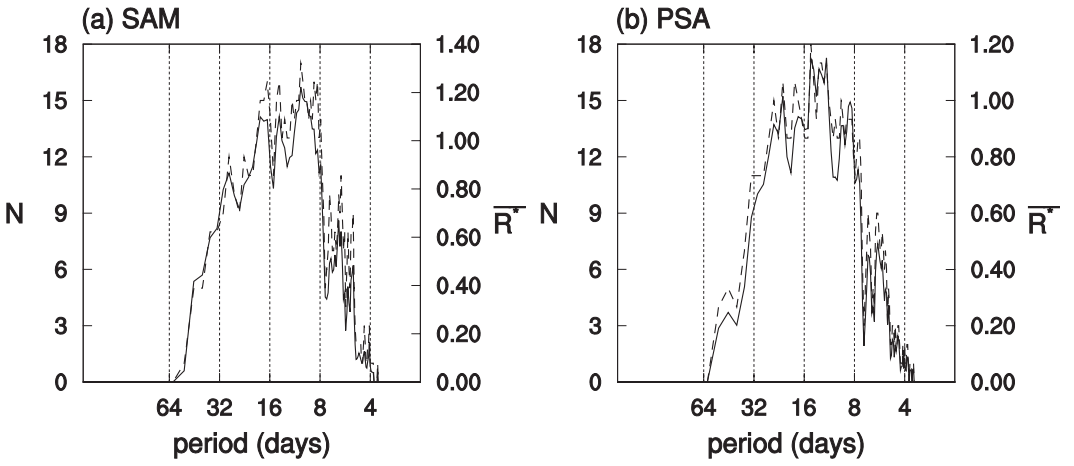

FIG. 7. (a),(b) As in Fig. 2, but for the daily SAM and PSA indices, respectively.

respectively. Both L_x and L_y denote east–west and north–south distances on the Mercator map, and are determined by the Mercator projection formulas, which transform longitude–latitude coordinates into Cartesian coordinates. For the extratropical region [the south–north extent is chosen as (80°–20°S) here to avoid the severe distortion near the South Pole in Mercator projection], L_x and L_y are approximately equal to $2\pi R$ and $2R$, respectively. Substitution in (9) gives

$$\left.\begin{aligned} \omega &= k\left(\frac{\overline{u}_M}{R} - \frac{4\beta_M R}{4k^2 + \pi^2 l^2}\right), \\ T &= \frac{2\pi}{\omega}, \end{aligned}\right\}, \qquad (10)$$

where T is the time period. Equation (10) clearly indicates that the time periods of waves depend on their spatial scales. Therefore, we performed a theoretical analysis on conditions 2–4 (see section 3) using (10). In calculation, β_M is taken as approximately 7.8×10^{-12} m^{-1} s^{-1} for the long-term annual mean averaged over mid- and high latitudes.

For condition 2, the time periods of various zonal waves can be determined by substituting $l = 1$ into (10). Figure 9 shows the series of time periods as a function of k calculated under different background wind speeds. The zonal wavenumber 3 ($k = 3$) shows significant low-frequency variability, with $\overline{u}_M$ ranging from 20 to 30 m s^{-1} (the observational 300 hPa $\overline{u}_M$ averaged over SH mid-latitudes is around 22 m s^{-1}). The low-frequency property of zonal wavenumber 4 becomes evident when $\overline{u}_M$ is close to 20 m s^{-1}. The time periods for other zonal wavenumbers show high-frequency variability. These theoretical results are mostly in agreement with the diagnostic findings for condition 2, and demonstrate that the low-frequency ZW3 may be interpreted as a low-frequency eigenmode of atmospheric circulation in the SH.

For condition 3, substituting $k = 0$ into (10) gives $\omega = 0$, suggesting that the zonally symmetric circulations are usually stationary, as for SAM and the meridional tripole. This agrees partly with the results for condition 3. The theoretical analysis is not appropriate for larger meridional wavenumbers, indicating that the variability of relatively small meridional waves is affected by other factors.

Figure 10 shows the time periods calculated using (10) for different zonal and meridional wavenumbers (as in condition 4) under the observed zonal wind speed. For each zonal wavenumber, the time period decreases with an increase in meridional wavenumber from $l = 2$ to $l = 4$, implying the dipole as a preferred meridional structure for low-frequency modes. The time periods for wavenumbers (k, l) = (1–5, 2) are much longer at small zonal wavenumbers 1–3, especially at zonal wavenumber 2. This result is essentially consistent with the observational findings for condition 4, and further demonstrates that quasi-stationary planetary-scale waves with a meridional dipole structure may be low-frequency eigenmodes of the atmosphere.

TABLE 1. The leading Fourier modes in the SAM and PSA patterns and the associated expansion coefficients determined by the DFS expansion. Numbers within parentheses are zonal and meridional wavenumbers, respectively. The subscripts C and S denote cosine and sine waves in the zonal direction.

Teleconnection modes	Fourier modes	Coefficients (gpm)
SAM	$(0, 2)$, $(1, 2)_c$, $(3, 1)_c$, $(2, 2)_s$, $(2, 1)_c$	−20, −4, 3, 2, 2
PSA	$(1, 2)_c$, $(1, 2)_s$, $(2, 2)_s$, $(2, 1)_c$, $(3, 1)_c$	5.5, −5, −4.5, −2, −2

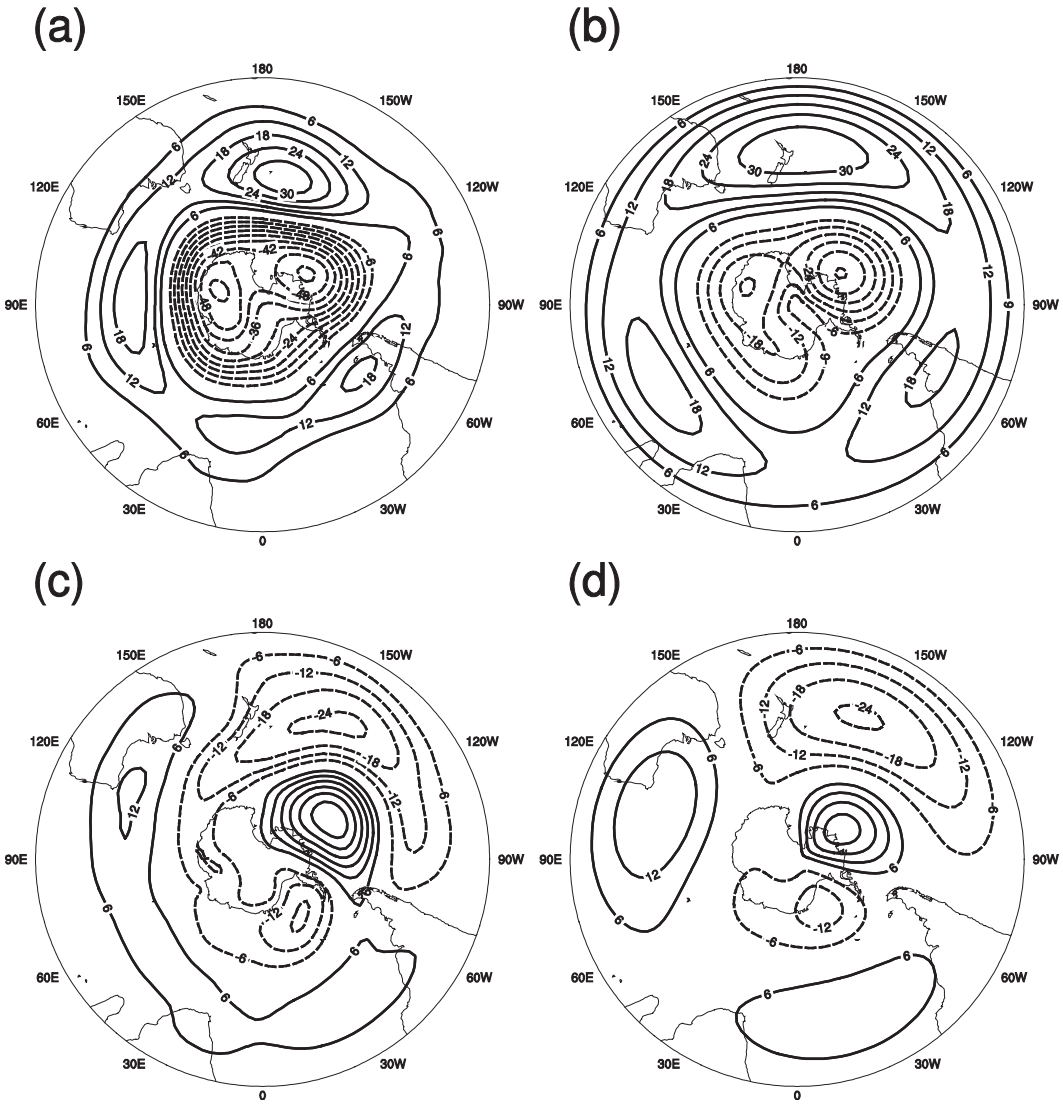

FIG. 8. (a) Regression of daily 500-hPa height anomalies onto the normalized daily SAMI. (b) Representation of (a) via the Fourier modes shown in Table 1. (c),(d) As in (a),(b), but for PSA. The contour interval is 6 gpm, and the solid and dashed lines indicate positive and negative anomalies, respectively; the zero lines are omitted.

5. Summary

This present paper analyzed the space–time spectral characteristics of the SH daily 500-hPa geopotential height by using a double Fourier series expansion and the standardized power spectrum. The Rossby dispersion relation was applied to partly interpret the diagnostic results.

Analyses of observational data over a 26-yr period yield the following results:

1) The extratropical-mean geopotential height follows a significant low-frequency periodicity of 10–30 days.
2) Among zonal waves (condition 2), zonal waves 3 and 4 show pronounced low-frequency variability, while waves of larger zonal wavenumbers mainly show high-frequency variability.
3) Among meridional waves (condition 3), the meridional dipole structure of zonally symmetric circulation is evident on the intraseasonal time scale, consistent with the time scale of SAM, and the meridional tripole also shows low-frequency variability.
4) Low-frequency 2D waves with large zonal scales favor a meridional dipole structure, indicating an out-of-phase relationship between planetary waves at mid- and high latitudes. Analysis of observational data over winter and summer half-years yields similar results to the analysis of entire years.

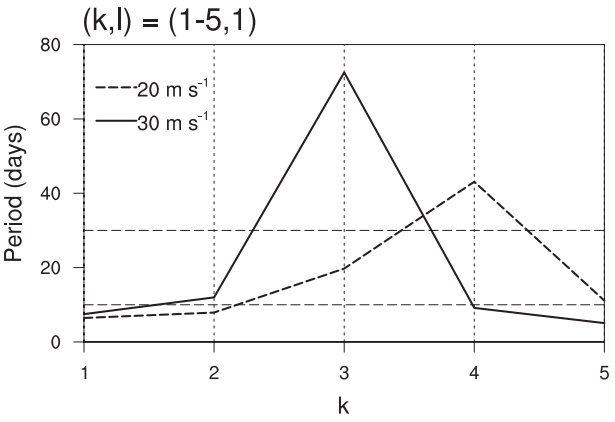

FIG. 9. Wave periods (days) for various zonal wavenumbers k calculated by (10) for condition 2 in basic flows of 20 m s^{-1} (dashed line) and 30 m s^{-1} (solid line). The two horizontal dashed lines stand for 10 and 30 days, respectively.

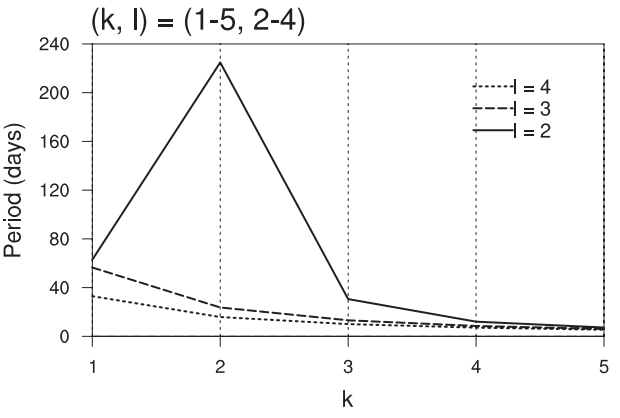

FIG. 10. Wave periods (days) for various zonal wavenumbers k calculated by (10) with meridional wavenumbers prescribed at l = 2 (solid line), l = 3 (dashed line), and l = 4 (dotted line).

The significant intraseasonal variability of both SAM and PSA is verified by standardized power spectrum analyses of their daily indices. Furthermore, the spatial-structure analyses indicate the dominant role of the meridional dipole structure in both SAM and PSA patterns, and that the dipole may be a preferred meridional structure for both zonally symmetric and asymmetric modes of low-frequency variability. In addition, the SAM and PSA modes contribute to the intraseasonal variability of the leading Fourier modes in their spatial patterns, further demonstrating the findings of the space–time spectral analyses.

A theoretical analysis was employed to qualitatively interpret the diagnostic results. Using the dispersion relation, we find that ZW3, meridional waves for $k = 0$ such as SAM, and planetary waves for $(k, l) = (1–3, 2)$ of low-frequency variability may be interpreted as low-frequency eigenmodes of the atmosphere. This analysis also provides a preliminary theoretical evidence for the dominant role of the meridional dipole in the intraseasonal teleconnection pattern, such as the PSA.

Our present results are preliminary, and further study is required to verify the meridional dipole structure of planetary waves using monthly- or seasonal-mean data. The present study focused on the temporal characteristics of modes over various spatial scales, but it is also necessary to examine the propagation features associated with these modes, especially waves with different meridional structures, which are important to our understanding the dynamics of teleconnection modes. The space–time spectral analysis over the northern extratropics (Sun and Li 2011) shows zonal wavenumbers 1 and 2 make larger contributions to the low-frequency variability than zonal wavenumber 3, which is inconsistent with the situation over the southern extratropics. It is necessary to examine whether differences in the space–time spectral characteristics of zonal waves between the NH and SH are related to differences in the land–sea distribution between the hemispheres. In addition, there is a lack of analysis of physical processes related to the observational time scales of teleconnection patterns. The time periods for low-frequency eigenmodes, such as SAM, appear to be stationary (or quasi-stationary); however, our observational analysis indicates that they have a low-frequency band of 10–30 days. This band may result from other complicated factors, such as wave–flow interactions (Lorenz and Hartmann 2001; Rashid and Simmonds 2004; Jin et al. 2006a,b). Moreover, this band represents an important time scale for those attempting to improve numerical weather forecasting (Baumhefner 1996).

Acknowledgments. We wish to thank three anonymous reviewers, whose comments and suggestions substantially improved the quality of this paper. Funding for this research was provided jointly by the 973 program (2010CB950400) and the NSFC Key Project (41030961).

REFERENCES

Baumhefner, D. P., 1996: Numerical extended-range prediction: Forecast skill using a low-resolution climate model. *Mon. Wea. Rev.,* **124,** 1965–1980.

Blackmon, M. L., 1976: Climatological spectral study of 500 mb geopotential height of Northern Hemisphere. *J. Atmos. Sci.,* **33,** 1607–1623.

——, Y. H. Lee, and J. M. Wallace, 1984: Horizontal structure of 500-mb height fluctuations with long, intermediate and short-time scales. *J. Atmos. Sci.,* **41,** 961–979.

Blunden, J., D. S. Arndt, and M. O. Baringer, Eds., 2011: State of the Climate in 2010. *Bull. Amer. Meteor. Soc.,* **92,** S1–S266.

Cai, W. J., and I. G. Watterson, 2002: Modes of interannual variability of the Southern Hemisphere circulation simulated by the CSIRO climate model. *J. Climate,* **15,** 1159–1174.

Cheong, H. B., 2000: Double Fourier series on a sphere: Applications to elliptic and vorticity equations. *J. Comput. Phys.,* **157,** 327–349.

——, 2006: A dynamical core with double Fourier series: Comparison with the spherical harmonics method. *Mon. Wea. Rev.,* **134,** 1299–1315.

——, I. H. Kwon, and T. Y. Goo, 2004: Further study on the high-order double-Fourier-series spectral filtering on a sphere. *J. Comput. Phys.,* **193,** 180–197.

Codron, F., 2007: Relations between annular modes and the mean state: Southern Hemisphere winter. *J. Atmos. Sci.,* **64,** 3328–3339.

Dell'Aquila, A., P. M. Ruti, S. Calmanti, and V. Lucarini, 2007: Southern Hemisphere midlatitude atmospheric variability of the NCEP-NCAR and ECMWF reanalyses. *J. Geophys. Res.,* **112,** D08106, doi:10.1029/2006JD007376.

Fan, K., 2007: Zonal asymmetry of the Antarctic Oscillation. *Geophys. Res. Lett.,* **34,** L02706, doi:10.1029/2006GL028045.

Feng, J., J. Li, and Y. Li, 2010: Is there a relationship between the SAM and southwest Western Australian winter rainfall? *J. Climate,* **23,** 6082–6089.

Frederiksen, J. S., and P. J. Webster, 1988: Alternative theories of atmospheric teleconnections and low-frequency fluctuations. *Rev. Geophys.,* **26,** 459–494.

Gerber, E. P., L. M. Polvani, and D. Ancukiewicz, 2008: Annular mode time scales in the Intergovernmental Panel on Climate Change Fourth Assessment Report models. *Geophys. Res. Lett.,* **35,** L22707, doi:10.1029/2008GL035712.

Gong, D. Y., and S. W. Wang, 1999: Definition of Antarctic Oscillation Index. *Geophys. Res. Lett.,* **26,** 459–462.

Gong, T. T., S. B. Feldstein, and D. H. Luo, 2010: The impact of ENSO on wave breaking and southern annular mode events. *J. Atmos. Sci.,* **67,** 2854–2870.

Hansen, A. R., and A. Sutera, 1991: Planetary-scale flow regimes in midlatitudes of the Southern Hemisphere. *J. Atmos. Sci.,* **48,** 952–964.

Hayashi, Y., 1979: Generalized method of resolving transient disturbances into standing and traveling waves by space-time spectral analysis. *J. Atmos. Sci.,* **36,** 1017–1029.

Hoskins, B. J., and D. J. Karoly, 1981: The steady linear response of a spherical atmosphere to thermal and orographic forcing. *J. Atmos. Sci.,* **38,** 1179–1196.

Jin, F. F., L. L. Pan, and M. Watanabe, 2006a: Dynamics of synoptic eddy and low-frequency flow interaction. Part I: A linear closure. *J. Atmos. Sci.,* **63,** 1677–1694.

——, ——, and ——, 2006b: Dynamics of synoptic eddy and low-frequency flow interaction. Part II: A theory for low-frequency modes. *J. Atmos. Sci.,* **63,** 1695–1708.

Jones, D. A., and I. Simmonds, 1993: Time and space spectral analyses of Southern Hemisphere sea level pressure variability. *Mon. Wea. Rev.,* **121,** 661–672.

Kanamitsu, M., W. Ebisuzaki, J. Woollen, S. K. Yang, J. J. Hnilo, M. Fiorino, and G. L. Potter, 2002: NCEP-DOE AMIP-II Reanalysis (R-2). *Bull. Amer. Meteor. Soc.,* **83,** 1631–1643.

Kao, S. K., 1968: Governing equations and spectra for atmospheric motion and transports in frequency wave-number space. *J. Atmos. Sci.,* **25,** 32–38.

Keable, M., I. Simmonds, and K. Keay, 2002: Distribution and temporal variability of 500 hPa cyclone characteristics in the Southern Hemisphere. *Int. J. Climatol.,* **22,** 131–150.

Kidson, J. W., 1988: Indices of the Southern Hemisphere zonal wind. *J. Climate,* **1,** 183–194.

——, 1999: Principal modes of Southern Hemisphere low-frequency variability obtained from NCEP–NCAR reanalyses. *J. Climate,* **12,** 2808–2830.

Layton, A. T., and W. F. Spotz, 2003: A semi-Lagrangian double Fourier method for the shallow water equations on the sphere. *J. Comput. Phys.,* **189,** 180–196.

Li, J. P., and J. L. X. L. Wang, 2003: A modified zonal index and its physical sense. *Geophys. Res. Lett.,* **30,** 1632, doi:10.1029/2003GL017441.

Li, X. F., and J. P. Li, 2009: Main submonthly timescales of Northern and Southern Hemispheres annular modes (in Chinese with English abstract). *Chin. J. Atmos. Sci.,* **33** (2), 215–231.

Lorenz, D. J., and D. L. Hartmann, 2001: Eddy-zonal flow feedback in the Southern Hemisphere. *J. Atmos. Sci.,* **58,** 3312–3327.

Meneghini, B., I. Simmonds, and I. N. Smith, 2007: Association between Australian rainfall and the Southern Annular Mode. *Int. J. Climatol.,* **27,** 109–121.

Mo, K. C., and G. H. White, 1985: Teleconnections in the Southern Hemisphere. *Mon. Wea. Rev.,* **113,** 22–37.

——, and M. Ghil, 1987: Statistics and dynamics of persistent anomalies. *J. Atmos. Sci.,* **44,** 877–901.

——, and R. W. Higgins, 1998: The Pacific–South American modes and tropical convection during the Southern Hemisphere winter. *Mon. Wea. Rev.,* **126,** 1581–1596.

——, and J. N. Paegle, 2001: The Pacific–South American modes and their downstream effects. *Int. J. Climatol.,* **21,** 1211–1229.

Nan, S., and J. P. Li, 2003: The relationship between the summer precipitation in the Yangtze River valley and the boreal spring Southern Hemisphere annular mode. *Geophys. Res. Lett.,* **30,** 2266, doi:10.1029/2003GL018381.

North, G. R., F. J. Moeng, T. L. Bell, and R. F. Cahalan, 1982: The latitude dependence of the variance of zonally averaged quantities. *Mon. Wea. Rev.,* **110,** 319–326.

Pezza, A. B., H. A. Rashid, and I. Simmonds, 2012: Climate links and recent extremes in Antarctic sea ice, high-latitude cyclones, Southern Annular Mode and ENSO. *Climate Dyn.,* **38,** 57–73.

Pohl, B., N. Fauchereau, C. J. C. Reason, and M. Rouault, 2010: Relationships between the Antarctic Oscillation, the Madden–Julian oscillation, and ENSO, and consequences for rainfall analysis. *J. Climate,* **23,** 238–254.

Randel, W. J., 1988: The seasonal evolution of planetary-waves in the Southern-Hemisphere stratosphere and troposphere. *Quart. J. Roy. Meteor. Soc.,* **114,** 1385–1409.

Raphael, M. N., 2004: A zonal wave 3 index for the Southern Hemisphere. *Geophys. Res. Lett.,* **31,** L23212, doi:10.1029/2004GL020365.

Rashid, H. A., and I. Simmonds, 2004: Eddy–zonal flow interactions associated with the Southern Hemisphere annular mode: Results from NCEP–DOE reanalysis and a quasi-linear model. *J. Atmos. Sci.,* **61,** 873–888.

Schneider, D. P., E. J. Steig, and J. C. Comiso, 2004: Recent climate variability in Antarctica from satellite-derived temperature data. *J. Climate,* **17,** 1569–1583.

Shutts, G. J., 1983: The propagation of eddies in diffluent jetstreams—Eddy vorticity forcing of blocking flow-fields. *Quart. J. Roy. Meteor. Soc.,* **109,** 737–761.

Simmonds, I., 2003: Modes of atmospheric variability over the Southern Ocean. *J. Geophys. Res.,* **108,** 8078, doi:10.1029/2000JC000542.

——, and J. C. King, 2004: Global and hemispheric climate variations affecting the Southern Ocean. *Antarct. Sci.,* **16,** 401–413.

Sun, C., and J. P. Li, 2011: Temporal-spatial spectral analysis of the Northern Hemisphere 500-hPa geopotential height (in Chinese with English abstract). *Chin. J. Atmos. Sci.,* **35** (6), 1079–1090.

Thompson, D. W. J., and J. M. Wallace, 2000: Annular modes in the extratropical circulation. Part I: Month-to-month variability. *J. Climate,* **13,** 1000–1016.

Trenberth, K. E., 1980: Planetary waves at 500 mb in the Southern Hemisphere. *Mon. Wea. Rev.,* **108,** 1378–1389.

——, and K. C. Mo, 1985: Blocking in the Southern Hemisphere. *Mon. Wea. Rev.,* **113,** 3–21.

Turner, J., 2004: The El Niño–Southern Oscillation and Antarctica. *Int. J. Climatol.,* **24,** 1–31.

van Loon, H., and R. L. Jenne, 1972: The zonal harmonic standing waves in the Southern Hemisphere. *J. Geophys. Res.,* **77,** 992–1003.

Wang, H. J., J. Q. Sun, and J. Z. Su, 2008: The northern annular mode: More zonal symmetric than the southern annular mode. *Chin. Sci. Bull.,* **53,** 1740–1744.

Wu, Z. W., J. P. Li, B. Wang, and X. H. Liu, 2009: Can the Southern Hemisphere annular mode affect China winter monsoon? *J. Geophys. Res.,* **114,** D11107, doi:10.1029/2008JD011501.